Light Intensity Modulated Impedance Spectroscopy (LIMIS) in All-Solid-State Solar Cells at Open Circuit

Osbel Almora[1,2,3]*, Yicheng Zhao[1], Xiaoyan Du[1], Thomas Heumueller[1], Gebhard J. Matt[1], Germà Garcia-Belmonte[3] and Christoph J. Brabec[1]

[1]*Institute of Materials for Electronics and Energy Technology (i-MEET), Friedrich-Alexander-Universität Erlangen-Nürnberg, 91058 Erlangen, Germany;*

[2]*Erlangen Graduate School in Advanced Optical Technologies (SAOT), Friedrich-Alexander-Universität Erlangen-Nürnberg, 91052 Erlangen, Germany*

[3]*Institute of Advanced Materials (INAM), Universitat Jaume I, 12006 Castelló, Spain*

*osbel.almora@fau.de

Keywords: impedance spectroscopy, solar cells, light intensity modulation, photocurrent, perovskite solar cells.

Abstract

Potentiostatic impedance spectroscopy (IS) is a well stablished characterization technique for elucidating the electric resistivity and capacitive features of materials and devices. In the case of solar cells, by applying a small voltage perturbation the current signal is recorded and the recombination processes and defect distributions are among the typical outcomes in IS studies. In this work a photo-impedance approach, named "light intensity modulated impedance spectroscopy" (LIMIS), is first tested in all-solid-state photovoltaic cells by recording the individual photocurrent (IMPS) and photovoltage (IMVS) responsivity signals due to a small light perturbation at open-circuit (OC), and combining them: LIMIS=IMVS/IMPS. The experimental LIMIS spectra from silicon, organic, and perovskite solar cells are presented and compared with IS. An analysis of the equivalent circuit numerical models for total resistive and capacitive features is discussed. Our theoretical findings show a correction to the lifetimes evaluations by obtaining the total differential resistances and capacitances combining IS and LIMIS measurements. This correction addresses the discrepancies among different techniques, as shown with transient photovoltage. The experimental differences between IS and LIMIS (i) proves the unviability of the superposition principle, (ii) suggest a bias-dependent photo-current correction to the empirical Shockley equation of the steady-state current at different illumination intensities around OC and (iii) are proposed as a potential figure of merit for characterizing performance and stability of solar cells. In addition, new features are reported for the low-frequency capacitance of perovskite solar cells, measured by IS and LIMIS.

1. Introduction

Standard potentiostatic impedance spectroscopic (IS) is a well-known and stablished technique for the characterization of the resistive, capacitive and inductive features of materials and solar cells.[1, 2] In photovoltaic devices, one of the most common characterization routines is to probe the open-circuit (OC) condition under an steady-state illumination intensity and by applying a small voltage perturbation at different light intensities the IS spectra are measured and analyzed. In this way the recombination resistance R_{rec}, chemical capacitance C_{μ} and characteristic lifetimes τ are typically accessed.

With an alternative approach, the photo-sensitive samples have been earlier separately characterized by means of the intensity modulated photocurrent spectroscopy (IMPS)[3-14] and the intensity modulated photovoltage spectroscopy (IMVS).[9, 10, 15-17] Particularly, the IMPS has been recently gaining attention in the field of perovskite solar cells (PSCs), mainly exploring the short-circuit (SC) condition.[13, 14, 18-20] IMVS and IMPS individually characterize the current and voltage responsivities Ψ_J and Ψ_V, respectively. Here a mere dimension analysis suggests that IMVS/IMPS has units of Ohms, like the impedance Z from IS. Therefore, it may be interesting to analyze IS and this ratio, here-on called light intensity modulated impedance spectroscopy (LIMIS). Purposely, Song & Macdonald[21] first introduced and measured the concept on n-Si in KOH solution, validating the transfer function by Kramers-Kronig transformation. Also Halme[22] tackled the subject and measured IMVS/IMPS in dye sensitized solar cells, concluding the approximate equivalence with IS. More recently, Bertoluzzi & Bisquert[12] mentioned the concept but only analyzed separately IMVS,

IMPS and IS in water splitting systems. Simultaneously to this work, we have proposed an analytical model which shows the difference between LIMIS and IS to be proportional to the surface recombination velocity.[23]

In this article we further analyze this concept at OC and first present an experimental analysis of LIMIS silicon,[24] organic[25, 26] and perovskite solar cells.[27, 28] The differences between IS and LIMIS spectra are introduced as a figure of merit for characterizing performance and degradation in solar cells. Our theoretical results suggest corrections to the concepts of differential resistance R and capacitance C for photosensitive samples under illumination. We show how by neglecting LIMIS the R and C can be over- and under-estimated, respectively, which ultimately corrects the assessment of charge carrier lifetimes. Our correction tackles the issue of the differences between experimental lifetime results from different techniques, as shown for transient photovoltage (TPV) profiles. The general equivalent circuit (EC) numerical model for the interpretation of the total R and C from photosensitive devices is also introduced, and the main differences in terms of EC fitting between IS and LIMIS are discussed. In addition, new capacitive features are reported for the low-frequency capacitance of PSCs. Finally, a bias-dependent photo-current correction is proposed to the empirical Shockley equation in order to conciliate the experimental observations and the theoretical deductions at OC for the steady-state current density-voltage $J-V$ curves at different light intensities.

In the following sections first IS and then LIMIS will be introduced in detail. The results are structured from the experimental reports to the theoretical deductions and analyses, and the conclusions are offered subsequently. Both theoretical and

experimental results are significantly complemented with the online supporting information. Note the list of acronyms, symbols and abbreviations in Table S1 in order to facilitate the reading.

1.1. Potentiostatic impedance spectroscopy (IS) in solar cells

We may first consider a generic sample at steady-state voltage $\overline{V}$ where a current density $\bar{J}(\overline{V})$ is flowing. In a first approximation, every sample can be assumed as a resistor-capacitor RC Voigt element with a characteristic time response constant $\tau = RC$, as in **Figure 1**a. Then a small potentiostatic perturbation $\widetilde{V}(t) = \left|\widetilde{V}\right|\exp[i\ \omega t]$ can be applied in alternating current (*ac*) mode, being t the time, ω the angular frequency and i the imaginary unit. The total voltage would be

$$V = \overline{V} + \left|\widetilde{V}\right|\exp[i\ \omega t] \tag{1}$$

Upon perturbation, the current may evolve as

$$J = \bar{J} + \tilde{J}\exp[i\ \omega t] \tag{2}$$

where $\bar{J}$ may be the steady-state current $\bar{J}(\overline{V})$ and the phasor-related part $\tilde{J}$ may inform on the differential resistive and capacitive features of the sample. A typical sinusoidal $\widetilde{V}(t)$ small perturbation is illustrated in **Figure 1**b, to which the current may be ϕ phase shifted, as in **Figure 1**c. Then we can write $\tilde{J} = \left|\tilde{J}\right|\exp[-i\phi]$ and the impedance can now be introduced as

$$Z(\omega) = \frac{\widetilde{V}(t)}{\tilde{J}(t)} = \frac{\left|\widetilde{V}\right|}{\left|\tilde{J}\right|}\exp[i\phi] \tag{3}$$

The ϕ-dependence on frequency $f = \omega/2\pi$ creates an impedance spectrum, which is the study subject of the impedance spectroscopy (IS). Most typically presented as $Z(\omega) = Z'(\omega) + i\ Z''(\omega)$, the Nyquist plot representation is illustrated in **Figure 1**d.

There the characteristic semicircle from a linear RC couple with single τ is shown. The real part Z' carries the information on the differential resistance, and since $\phi \to 0$ when $\omega \to 0$ thus $Z \to Z'$ and the total differential resistance can be taken as the radius of the semicircle. On the other hand, the imaginary part Z'' informs on the capacitive features. Note that the $-Z''$ maximum ($\phi = \pi/4$ in **Figure 1**d) belongs to the characteristic angular frequency $\omega_\tau = \tau^{-1} = (R \cdot C)^{-1}$.

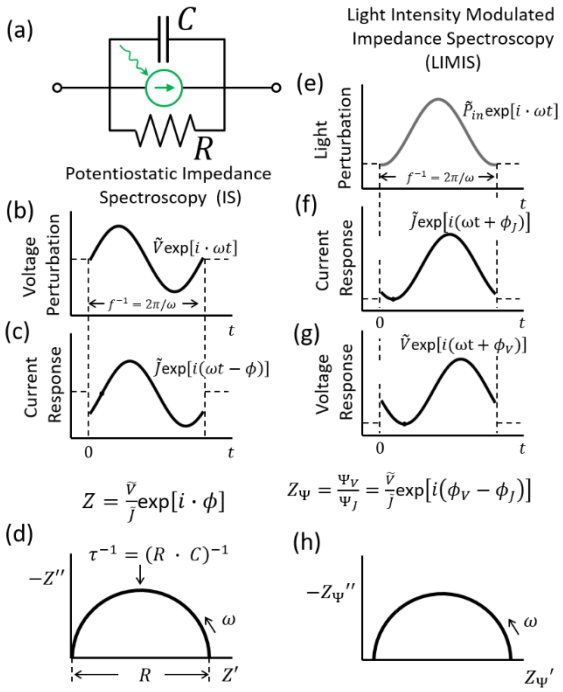

Figure 1. Schematized strategies for perturbation and characterization of electric responses from a solar cell as a (a) photo-sensitive simple RC Voigt circuit element: (b-d) IS and (e-h) LIMIS. For simplicity the modulus notation was avoided.

For a solar cell, the series resistance R_{series} and shunt resistance R_{sh} effects could be ideally neglected at forward bias, under illumination and around the open-circuit (OC) regime condition. In those circumstances the current density-voltage $J - V$ characteristic can be taken as the empirical approximation of the Shockley equation

$$J = J_s \left(\exp\left[\frac{q\,V}{m\,k_B T}\right] - 1\right) - J_{ph} \tag{4.a}$$

where q is the elementary electric charge, $k_B T$ the thermal energy, J_s the saturation current, m the ideality factor, and J_{ph} is the bias-independent photo-generated current, typically taken as the short-circuit current J_{sc}. Equation (4.a) characterizes the experimental measurement where the current is considered in steady state, i.e. direct current (*dc*) mode. Particularly, at open-circuit (OC) under forward *dc* biases larger than $5k_B T$ the expression (4.a) can be expressed in terms of the open circuit voltage V_{oc} reciprocity

$$J_{ph} \cong J_s \exp\left[\frac{q\,V_{oc}}{m\,k_B T}\right] = \Psi_J P_{in} \tag{4.b}$$

where $\Psi_J = \Psi_{sc}$ is the photo-current responsivity at short-circuit that depends on the incident light spectrum, the absorption coefficient and the geometry of the absorbing materials, and P_{in} is the incident light intensity in units of power density. Experimentally, under *ac* potentiostatic perturbation (IS measurement) the current signal results from evaluating (4.a) in (1), sampling the narrow region around the steady state condition. **Figure 2**a illustrates the particular case where OC is tested at constant illumination intensity.

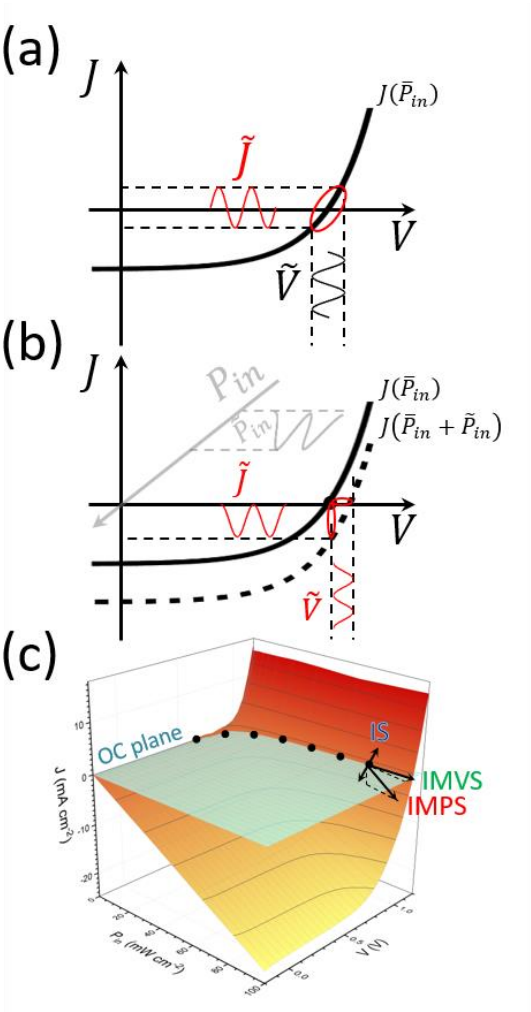

Figure 2. Schematized impedance characterization of a photovoltaic solar cell in 2D $J-V$ representations for (a) IS and (b) LIMIS. The thick dashed line in (b) is the projection of the perturbed $J(V,P_{in})$ curve in the 3D representation, as in (c). In (c) the three experimental measurement are illustrated at an OC point in the interception between the 3D $J(V,P_{in})$ surface and the OC plane: where LIMIS takes place.

1.2. Light intensity modulated impedance spectroscopy (LIMIS) in solar cells

Alternatively to the IS approach, in the case of photo-sensitive samples (see **Figure 1**a which included a photo-current source) the perturbation can be done by a light source. Then, a small perturbation $\widetilde{P}_{in}(t)=\left|\widetilde{P}_{in}\right|\exp[i\,\omega t]$ can be added to the given

dc incident light power density $\overline{P}_{in}$, as in **Figure 1**e. The total incident light intensity in units of power density would be

$$P_{in} = \overline{P}_{in} + \left|\widetilde{P}_{in}\right|\exp[i\ \omega t] \tag{5}$$

Upon this perturbation, both current and voltage signals can be recorded. At a given $\overline{V}$, the current would be ϕ_J phase shifted, as in **Figure 1**f, and similarly to (2) $\tilde{J} = \left|\tilde{J}\right|\exp\left[i\phi_J\right]$. Hence a current responsivity transfer function can be defined as

$$\Psi_J(\omega) = \frac{\tilde{J}}{\widetilde{P}_{in}} = \frac{\left|\tilde{J}\right|}{\left|\widetilde{P}_{in}\right|}\exp\left[i\phi_J\right] \tag{6}$$

Likewise, at OC ($J = 0$) the photovoltage signal may be composed by the *dc* open circuit voltage $\overline{V}_{oc}$ and the phasor related part as

$$V_{oc} = \overline{V}_{oc} + \widetilde{V}_{oc}\exp[i\ \omega t] \tag{7}$$

Then the photo-voltage signal may have a phase shift ϕ_V (see **Figure 1**g) and taking $\widetilde{V}_{oc} = \left|\widetilde{V}_{oc}\right|\exp[i\phi_V]$ thus a voltage responsivity transfer function is defined as

$$\Psi_V(\omega) = \frac{\widetilde{V}_{oc}}{\widetilde{P}_{in}} = \frac{\left|\widetilde{V}_{oc}\right|}{\left|\widetilde{P}_{in}\right|}\exp[i\phi_V] \tag{8}$$

Equations (6) and (8) define by themselves IMPS and IMVS, respectively. These techniques have been earlier introduced[3-6, 12, 16, 29] and there have been recent studies on photovoltaic solar cells.[10, 11, 13, 17, 30]

However, there are three main limiting factors when using individually IMPS or IMVS. First, the placing of a current (voltage) source for IMPS (IMVS) in the equivalent circuit (EC) is a particularly challenging task given that implies a direct impact in the distribution of currents and/or voltages which is not so straightforward

in practice. This is an additional complication to the already debated selecting and justifying of using a given EC in IS, only with resistive and capacitive elements. Second, IMPS or IMVS cannot reproduce resistance or capacitance spectra, which limits it use in already stablished techniques like thermal admittance spectroscopy (TAS).[31] And last but not least, the validation of IMPS or IMVS with IS results is not so straightforward since each photo technique lacks one component or the other in terms of conductivity or field distribution.

Now, IMPS and IMVS can be combined to obtain the "light intensity modulated impedance spectroscopy" (LIMIS)

$$Z_{\Psi}(\omega) = \frac{\Psi_V}{\Psi_J} = \frac{\left|\widetilde{V}_{oc}\right|}{\left|\tilde{J}\right|}\exp\left[i\left(\phi_V - \phi_J\right)\right] = |Z_{\Psi}|\exp[i\phi_{\Psi}] \quad (9)$$

Advantageously, the experimental spectra from the photo-impedance of (9) do not need voltage/current sources in the EC-based numerical simulations, resulting a simpler and less ambiguous task. Also the spectroscopic representation of the resistive (see **Figure 1**h) and capacitive features can be obtained too, which allows future development of analogue light intensity modulated thermal admittance spectroscopy (LIMTAS). And furthermore, a LIMIS direct comparison with IS spectra may straightforwardly inform on generation/recombination features in solar cells.

Figure 2b presents a scheme on the LIMIS concept for typical photovoltaic cells -with $J-V$ characteristic as (4.a)- at OC under illumination. Despite the sampled *dc* condition is the same as for the IS (**Figure 2**a), LIMIS perturbates the steady-state in a third axis, corresponding to the incoming illumination power density P_{in}. As a result, the current and voltage signals spread individually, each one exclusively in the

direction of its own axis. The thick dashed line in **Figure 2**b represent the 2-dimentional (2D) projection of the perturbated current, and **Figure 2**c shows the Equation (4.a) approximation for the family of 3-dimentional (3D) $J-V$ curves which are sampled when modulating incident light intensity. Also in **Figure 2**c the three separately examples of measurements are indicated: (i) IS in a *J*-*V* plane at a fixed P_{in}, (ii) IMPS in a $J-P_{in}$ plane at a fixed V (short-circuit in the figure), and (iii) IMVS in the $V-P_{in}$ plane at open circuit, named OC surface.

Importantly, in the core of our focus is to provide a first approach to the difference between LIMIS and IS, its meaning and possible use. Accordingly, herein we define a normalized figure of merit called photo-impedance difference as

$$\Delta Z_{\Psi}=\frac{Z_{\Psi}-Z}{Z} \tag{10}$$

where Z and Z_{Ψ} come after (3) and (9), respectively. Note that ΔZ_{Ψ} is zero when $Z_{\Psi}=Z$ and positive (negative) when the photo-impedance from LIMIS is larger (lower) than that from IS.

2. Results and discussion

2.1. Experimental LIMIS and IS spectra

A proper analysis between IS and LIMIS at OC requires to set the same steady-state *dc* illumination intensity. Subsequently IMVS can be measured directly at OC and for IS and IMPS the forward bias corresponding to the same V_{oc} should be applied so the J_{sc} is cancelled. For IMPS and IMVS, the exact set of sampled frequencies is an obvious requirement. Other external parameters like temperature, humidity (when

reactivity issues) or even the wire connections should be controlled to be the same during the three measurements, so the characterized state is nearly the same.

The IS, IMPS and IMVS measurements were carried out with the Zahner Zennium Pro/PP211 impedance setup using its LSW-2 white LED light source. In all cases the sample holder included N_2 atmosphere.

Notably, ensuring the requirement of linear small perturbation is of upmost importance, mainly when measuring IMPS and IMVS to obtain LIMIS. In the case of IS, typically $\widetilde{V} < k_B T/q$ delivers accurate results, and for IMPS and IMPV keeping the *ac* perturbation below 10% of *dc* light intensity ($\widetilde{P}_{in} < \overline{P}_{in}/10$) provides a good empirical reference too. However, the latter rule can be not good enough in some cases, particularly for low *dc* illuminations approaching the *ac* experimental setup limit. Therefore, we use a significance parameter as described by Schiller and Kaus[32] and automatically implemented in the Zahner setup. The significance parameter goes from 0 to 1 and informs of "perfect linearity" if it equals unity. In practice, optimal results should be abode 0.98 and those below 0.95 should be discarded.

Five representative samples were experimentally characterized as summarized in Section S1.1: a silicon solar cell SiSC, an organic solar cell (OrgSC) and three perovskite solar cells (PSC1,2,3). The respective schemed structures, $J-V$ curves, external quantum efficiency (EQE) spectra and 500 hours degradation tests (for the PSCs) are in Figure S1. The performance parameters are in Table S2.

The silicon device constitutes the first reference due to the simplicity and robustness of its working principles. Its characterization is presented in Section S1.2: first the

IMPS and IMVS spectra at OC under different *dc* illumination intensities in Figure S2, and then LIMIS and IS spectra for the SiSC are shown in Figure S3. The current and voltage responsivities in Figure S2 illustrate the expected arc-like shapes in the Nyquist representation. In **Figure 3**a the low frequency limits from Ψ_V and Ψ_J are plotted. From IMVS the relation $\Psi_V = mk_BTq^{-1}{P_{in}}^{-1}$ with $m \approx 1.3$ is in agreement with theoretical predictions[16, 23] and the photocurrent-photovoltage trend in Figure S4a. On the other hand, from IMPS the light-intensity independency of Ψ_J in almost all the range of measurement seems to fade only as V_{oc} approaches the built-in voltage V_{bi}, illustrated in the Mott-Schottky plot of Figure S4b.

By applying the LIMIS definition (9) the photo-impedance spectra can be compared with the standard IS spectra, as in Figure S3 and **Figure 3**b. A right-shifted Nyquist plot is apparent, reporting $\Delta Z_\Psi > 0$ in the measured range. For the sake of clarity, this series-resistance-like right-shift in the real part of the LIMIS impedance is going to be referred in the next as ${Z_s}'$.

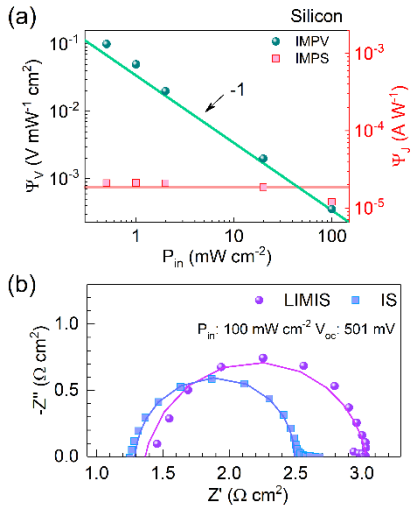

Figure 3. Silicon solar cell spectroscopic characterization: (a) low frequency limits of the voltage and current responsivities for different light intensities (see Figure

S2) and (b) representative impedance Nyquist plot (see Figure S3). Lines in (a) belong to fitting to $\Psi_V \propto {P_{in}}^{-1}$and $\Psi_J \propto {P_{in}}^{0}$, and in (b) refers to the EC model discussed in Section 2.3 and **Figure 7**b.

The organic device, with structure ITO/ZnO/PM6:Y6/MoOx/Ag, was characterized as presented in Section S1.3 including the device fabrication description. Similarly, Figure S5 shows the IMPS and IMVS spectra and Figure S6 the comparison between IS and LIMIS.

Figure 4a presents the low frequency limits of the voltage and current responsivities spectra for the OrgSC. From the IMVS, $\Psi_V = mk_BTq^{-1}{P_{in}}^{-1}$ with $m \approx 1.8$ is again in agreement with theoretical predictions[16, 23] and the photocurrent-photovoltage trend in Figure S4c. Differently, from the IMPS Ψ_J behaves more like $\Psi_J \propto {P_{in}}^{-1/3}$ in a low and medium range for the measured illumination intensities. Moreover, **Figure 4**b illustrate one of the Nyquist plots showing the similar arcs of the two techniques, also with the right-shifting trend for the LIMIS spectrum. More interestingly here it is that the apparent series resistance $Z_s{}'$ shows a negative arc in the Nyquist representation (empty dots in **Figure 4**b). This is an important feature whose understanding, while beyond the scope of this paper, should be attended in future works.

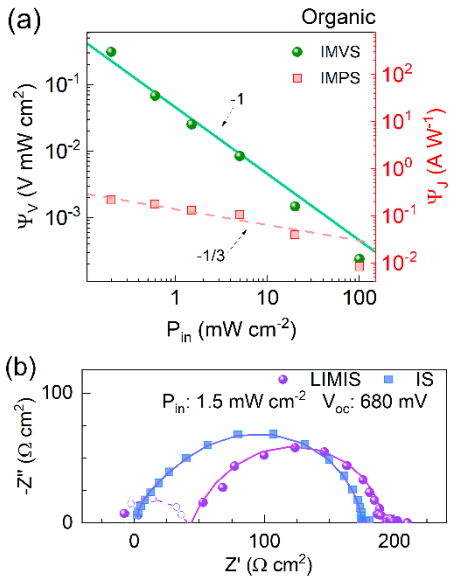

Figure 4. Organic solar cell spectroscopic characterization: (a) low frequency limits of the voltage and current responsivities for different light intensities (see Figure S5) and (b) representative impedance Nyquist plot (see Figure S6). Lines in (a) belong to fitting to $\Psi_V \propto {P_{in}}^{-1}$and $\Psi_J \propto {P_{in}}^{0}$(dashed line to $\Psi_J \propto {P_{in}}^{-1/3}$), and in (b) refers to the EC model discussed in Section 2.3 and **Figure 7**b. LIMIS empty dots in (b) mean negative values.

The perovskite solar cells under study all shared similar n-i-p structures, with variations in the absorber and the electron selective contact layers. Labeled as PSC1, we first discuss the spectroscopic characterization (see Section S1.4) of the more efficient and stable sample (see Section S1.1), with structure ITO/SnO_2/PMMA(PCBM)/$Cs_{0.05}MA_{0.1}FA_{0.85}Pb(I_{0.85}Br_{0.15})_3$/PDCBT/Ta-$WO_x$/Au. Similarly, the characterizations of PSC2 and PSC3, with structures ITO/SnO_2/$Cs_{0.05}MA_{0.1}FA_{0.85}Pb(I_{0.85}Br_{0.15})_3$/PDCBT/Ta-$WO_x$/Au and ITO/$SnO_2$/$Cs_{0.15}FA_{0.85}PbI_3$/PDCBT/Ta-$WO_x$/Au, are presented in sections S1.5 and S1.6, respectively.

The IMPS and IMVS spectra for PSC1 are presented in Figure S8, evidencing already a more complex response including two arcs in the Nyquist plots. Regarding the low

frequency limits of the voltage and current responsivities from PSC1, in **Figure 5**a, the IMVS similarly gives $\Psi_V = mk_BTq^{-1}{P_{in}}^{-1}$ with now $m \approx 1.5$ following theory[16, 23] and agreeing previous reports on ideality factors from mixed cation PSCs.[33, 34] Distinctly, the IMPS reports a situation somehow in the middle between constant Ψ_J at lower light intensities and $\Psi_J \propto {P_{in}}^{-1/3}$ at higher illuminations. The latter resembles the behavior of the OrgSC, probably related with the intrinsic absorber nature of both.

Applying LIMIS definition (9) allows to compare it with the IS spectra, as in Figure S9. PSC1 brings a new feature to the impedance spectra by reporting a clear three RC constants, i.e., three arcs in the Nyquist plots and three steps in the capacitance Bode plots. Importantly, as illustrated in **Figure 5**b, the high frequency region of the spectra (f>1kHz) from LIMIS delivers negative values in the Nyquist plot (empty dots) and a consequent negative capacitance in the Bode plots of Figure S9. Hence, the expected high frequency arcs (plateau) of the LIMIS impedance (capacitance) spectra from PSCs are not so and instead suggest a higher complexity in terms of EC elements. The high frequency region from IS reproduces earlier described features.[35, 36] On the other hand, at low frequencies (f<1kHz) LIMIS seems to reproduce very well the IS spectra, in both the impedance Nyquist plot (2 arcs in **Figure 5**b) and the capacitance Bode plot (2 steps in **Figure 5**c).

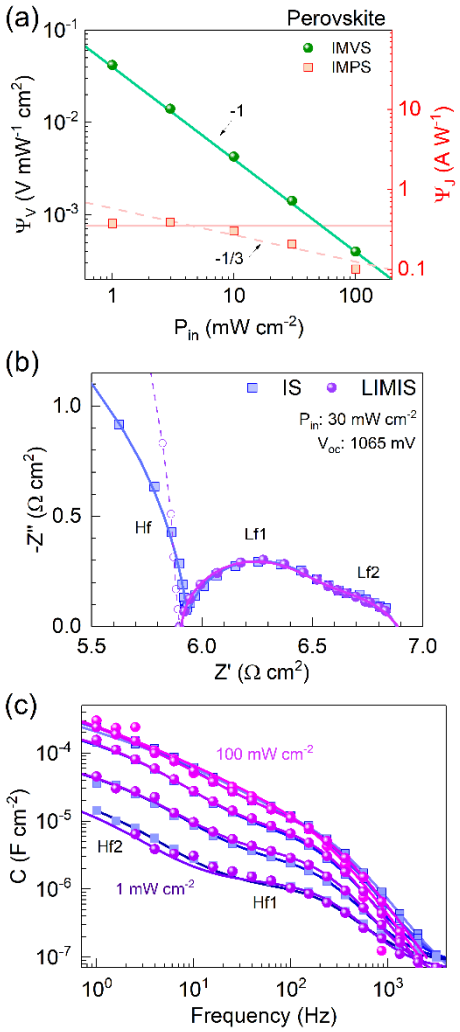

Figure 5. Perovskite solar cell (PSC1) spectroscopic characterization: (a) low frequency limits of the voltage and current responsivities for different light intensities (see Figure S2) and (b) representative impedance Nyquist plot (see Figure S3). Lines in (a) belong to fitting to $\Psi_V \propto P_{in}{}^{-1}$and $\Psi_J \propto P_{in}{}^{0}$(dashed line to $\Psi_J \propto P_{in}{}^{-1/3}$), and in (b) refers to the EC model discussed in Section 2.3 and **Figure 7**c. LIMIS empty dots in (b) mean negative values.

Moreover, one final interesting correlation is remarked regarding the comparison between LIMIS and IS in terms of ΔZ_Ψ. By taking the low frequency limit we can express it as $\Delta Z'_\Psi = (Z_T{}' - R_T)/R_T$ where Z'_T and R_T come from LIMIS and IS respectively. This is displayed in **Figure 6** for the set of studied devices. The general

trend shows first a decrease as light intensity is augmented until a few tens of mW·cm^{-2}. In this range a rough approximation would say that $Z_\Psi \propto Z\left(1 + {P_{in}}^{-2}\right)$. Towards 1 sun illumination intensity, the photo-impedance from LIMIS seems to exceed the impedance from IS as light intensity grows. In this latter range we could speculate that $Z_\Psi \propto Z\left(1 + {P_{in}}^{2}\right)$. Interestingly, in the region between the two regimes, some negative values are reported, indicating that the photo-resistance from LIMIS is lower that the total resistance from IS. This only occurs for the OrgSC, PSC2 and PSC3. These are actually the devices with more performance issues: the OrgSC presents "S" shape above OC and the PSC2 and PSC3, besides the lower PCE, and V_{oc}, showed lower stability too (see Figure S1). These correlations are also a matter of further analyses, but these preliminary observations suggest that the higher $\Delta Z'_\Psi$ the best, and that negative values of $\Delta Z'_\Psi$ indicate performance and/or degradation issues in solar cells.

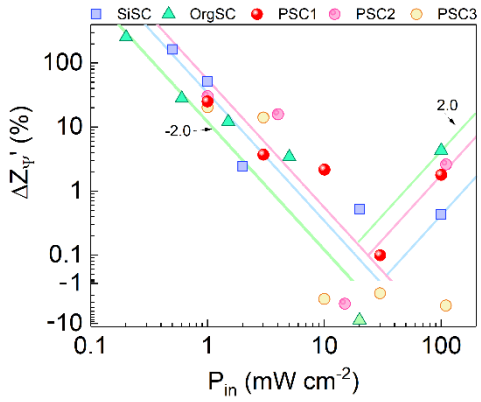

Figure 6. $\Delta Z'_\Psi$ as a figure of merit for checking performance and*or degradation issues: normalized real difference between Z'_T and R_T, from LIMIS and IS respectively, as a function of illumination intensity for the different studied devices. Only the cells with low performance or degradation issues show negative $\Delta Z'_\Psi$.

2.2. The differential approach to resistance and capacitance: correcting lifetimes

The derivative of the scalar current $J(V, P_{in})$ is measured in different directions $\hat{v}_1$, $\hat{v}_2$ and $\hat{v}_3$ by IS, IMPS and IMVS, respectively. Thus, we can calculate them by using the concept of directional derivative and the directions in the OC surface ($J = 0$). For IS the derivative is found in the direction of $\widetilde{V}$, so $\hat{v}_1 = (1,0)$ and for IMPS, in the direction of $\widetilde{P}_{in}$, so $\hat{v}_2 = (0,1)$. These are the well-known partial derivatives in the axes directions. However, IMVS is not a partial derivative of $J(V, P_{in})$ but V_{oc}. Hence we may redefine it as the directional derivative of $J(V, P_{in})$ in the direction $\hat{v}_3$ contained in the interception between the OC surface and $J(V, P_{in})$ (see **Figure 2**c). Consequently, we can now express the transfer functions of IS (3), IMPS (6), IMVS (8) and thus LIMIS (9) as derivatives at $\overline{V} = \overline{V}_{oc}$, respectively as

$$Z = \left(\vec{\nabla}_{\hat{v}_1} J\right)^{-1} = \left(\vec{\nabla} J \cdot (1,0)\right)^{-1} = \left(\frac{\partial J}{\partial V}\right)^{-1} \tag{11.a}$$

$$\Psi_J = \vec{\nabla}_{\hat{v}_2} J = \vec{\nabla} J \cdot (0,1) = \frac{\partial J}{\partial P_{in}} \tag{11.b}$$

$$\Psi_V = \vec{\nabla}_{\hat{v}_3} J = \vec{\nabla} J \cdot (v_{30}, v_{31}) = \frac{\partial V_{oc}}{\partial P_{in}} \tag{11.c}$$

$$Z_\Psi = \frac{\partial V}{\partial P_{in}} \left(\frac{\partial J}{\partial P_{in}}\right)^{-1} \tag{11.d}$$

Purposely, we are here interested in two main physical quantities: the total differential resistance unit area

$$R = \left(\frac{dJ}{dV}\right)^{-1} \tag{12}$$

and the total differential capacitance per unit area

$$C = \frac{dQ}{dV} \tag{13}$$

where Q is the charge density. Equations (12) and (13) are total differentials that can be approached to the partial derivatives from the potentiostatic IS following (11.a) as

$$R_{IS}(\omega) \approx \left(\frac{\partial J}{\partial V}\right)^{-1} = \mathrm{Re}[Z(\omega)] \tag{14.a}$$

$$C_{IS}(\omega) \approx \frac{\partial Q}{\partial V} = \mathrm{Re}\left[\frac{1}{i\ \omega\ Z(\omega)}\right] \tag{14.b}$$

where $Z(\omega)$ is that of (3) and $\partial Q \propto \partial J/\omega$ at each frequency. Definition (14) is the full form of (12) and (13) in dark measurements and for non-photosensitive samples.

An interesting exercise is to apply (14.a) to (4.a) in order to obtain the typically called *dc* resistance

$$R_{dc} = R_{th} \exp\left[-\frac{q\ V}{m\ k_B T}\right] \tag{15.a}$$

where $R_{th} = m\ k_B T/J_s q$ is the thermal recombination resistance. In practice, IS resolves the different ω-components in the resistive response from a sample, but the total resistance should resemble R_{dc} and converge in the appropriate low frequency limit. Note that at OC V should be substituted by V_{oc} in (15.a) and $R_{dc}(V) = R_{dc}(V_{oc})$ only if J_{sc} does not depend on bias.

We can also apply (11.b-d) to the empirical approximation of the Shockley equation (4) resulting the analogue *dc* parameters

$$\Psi_{J,dc} = -\Psi_J \tag{15.b}$$

$$\Psi_{V,dc} = \frac{m\ k_B T}{q\ P_{in}} \tag{15.c}$$

$$R_{\Psi,dc} = \frac{m\ k_B T}{q\ \Psi_J P_{in}} = R_{th}\ \exp\left[-\frac{q\ V}{m\ k_B T}\right] \tag{15.c}$$

where $\Psi_J = J_{sc}/P_{in}$ has the same meaning as in (4.b). Note that in the assumption of bias-independent Ψ_J, and in agreement with (4.b), $\Psi_J P_{in} = J_s \exp[qV/m\ k_B T]$ and thus $R_{dc} = R_{\Psi,dc}$. This equality expresses the dark/light superposition rule, following the reciprocity theorem of charge collection,[37] which implies that the $J-V$ curves under illumination are the same as the dark one, only current shifted an amount $-J_{sc}$.

Now, similarly to (14) for IS, the IMPS and IMVS respectively explore partial derivatives as in (11.b,c). This is illustrated in **Figure 2**c and left side of **Figure 2**d. Subsequently, since (4) is not light independent, the definition (12) can be better approached as

$$R = \left(\frac{\partial J}{\partial V} + \frac{\partial J}{\partial P_{in}}\frac{\partial P_{in}}{\partial V}\right)^{-1} \tag{16.a}$$

$$R(\omega) = \left(\frac{1}{\mathrm{Re}[Z(\omega)]} + \frac{1}{\mathrm{Re}[Z_\Psi(\omega)]}\right)^{-1} = \left(\frac{1}{R_{IS}(\omega)} + \frac{1}{R_\Psi(\omega)}\right)^{-1} \tag{16.b}$$

From (16), note that the predominant term will be the lower of the resistances R_{IS} and R_Ψ, from IS and LIMIS respectively. Also, from the *dc* approximation, if $R_{IS} \sim R_\Psi$ then R results around a half of that typically estimated from IS. This result is related with the typical photoconductivity enhancement in photovoltaic devices when comparing dark and light behavior by IS or even *dc* measurements. R is a measure of

how much current (dQ/dt) changes per unit change of voltage, and (16) express the light dependency of that ratio.

On the other hand, in the case of the capacitance, it makes sense to think that, some extra charge is stored in the device under illumination, different to what would be expected from the dark regime, even considering chemical capacitance effects. Accordingly, a better estimation of the differential capacitance in photosensitive samples would be

$$C = \frac{\partial Q}{\partial V} + \frac{\partial Q}{\partial P_{in}} \frac{\partial P_{in}}{\partial V} \tag{17.a}$$

$$C(\omega) = \mathrm{Re}\left[\frac{1}{i\ \omega\ Z(\omega)} + \frac{1}{i\ \omega\ Z_{\Psi}(\omega)}\right] = C_{IS}(\omega) + C_{\Psi}(\omega) \tag{17.b}$$

Similarly, from (17), note that the predominant term will be the larger of the capacitances C_{IS} and C_{Ψ}, from IS and LIMIS respectively. Specifically, if $C_{IS} \sim C_{\Psi}$ then C results twice that typically estimated from IS. As in the case of resistance, light charges the capacitor in addition to how the bias does it, hence it makes sense that some extra charge is stored. Accordingly, it is of crucial importance to evaluate the degree of overestimation (underestimation) of the differential resistance (capacitance) by only considering IS measurements.

Importantly, if the superposition rule (14) is valid, then $Z = Z_{\Psi}$ makes $R = R_{IS}/2$ and $C = 2C_{IS}$. Accordingly, the LIMIS measurements would not modify the corresponding characteristic response times $\tau = RC = R_{IS}C_{IS}$. For instance, this would be the case where the characteristic lifetimes from IS spectra coincide with some other techniques like TPV, as earlier reported.[38] However, as showed in the

previous section, we found $Z \sim Z_{\Psi}$ which may deliver a corrected lifetime including all the carrier contributions due to bias and light dependencies. Note that this result does not conflicts the reciprocity theorem of charge collection,[37] which states the equivalence between the currents due to photo-generation at a point surrounded by no charge and the injection of the same charge to the surrounding of the same point, if all the rest of boundary conditions in the space are kept the identical. Our findings of $Z \neq Z_{\Psi}$ just reflect how photo-generation modifies the boundary conditions with respect to dark recombination currents due to the injection of carriers.

2.3. Numeric approach: the equivalent circuits

After introducing LIMIS in Section 1.2, the total differential resistance and capacitance from photosensitive samples was corrected in Section 2.2, resulting as in equations (16) and (17). Differently to the that suggested by the derivatives of the *dc* empirical Shockley equation (15), our recent analytical analysis[23] suggested that the impedances from IS and LIMIS should differ. Accordingly, the accurate estimation of R and C may include the measurement of LIMIS. In particular, the incorporation of both concepts can be represented in an equivalent circuit (EC) as in **Figure 7**a, where the impedance Z from IS and the photo-impedance Z_{Ψ} from LIMIS are connected in parallel among them, excluding the non-photosensitive contributions from the ohmic series resistances R_{series}. Also in **Figure 7**a the simplest EC including a couple of Voigt elements in parallel is illustrated, in agreement with differential definitions (16) and (17).

IS and LIMIS are measured separately, and in the next section the experimental measurement will be presented and discussed. **Figure 7**b,c display the ECs used for

the numerical fitting indistinctively for IS and LIMIS. These are well-known widely used ECs for characterizing solar cells.[2, 33, 39] Note that even in cases where both techniques were fitted with the same EC, that does not mean that every element share the same physical meaning. In any case, from **Figure 7**b,c the total resistances either from IS or LIMIS are taken from the series connection as $R_T = R_{\mathrm{Hf}} + R_{\mathrm{Lf}}$ and the total capacitance, in parallel, as $C_T = C_{Hf} + C_{Lf}$. In most of the cases C_{Hf} will be the geometrical capacitance of the sample C_g, or the depletion layer capacitance C_{dl}. From these parameters, the characteristic times $\tau_{Hf} = C_{Hf}R_{\mathrm{T}}$ and $\tau_{Lf} = C_{Lf}R_{Lf}$ can be obtained and studied.

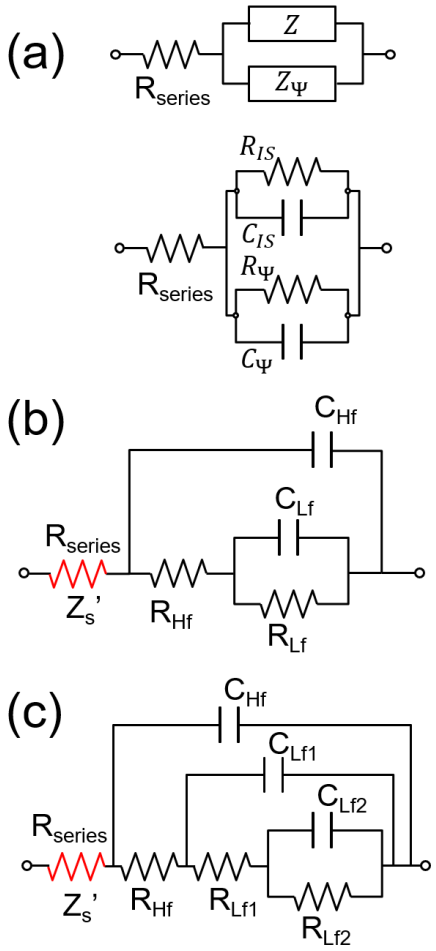

Figure 7. Equivalent circuits for (a) the concept of total differential contributions from IS and LIMIS to resistance and capacitance and (b, c) the used equivalent circuits during the numerical simulation of IS and LIMIS spectra. R_{series} is a series resistor, R_{IS} and R_{Ψ} are the total resistances measured by IS and LIMIS, R_{Hf} and R_{Lf} are high and low frequencies resistors, C_{IS} and C_{Ψ} are the total resistances measured by IS and LIMIS, and C_{Hf} and C_{Lf} are high and low frequencies capacitors, respectively.

For the silicon solar cell, the IS and LIMIS spectra were numerically simulated to the EC model of **Figure 7**b as presented with solid lines in Figure S3 and **Figure 3**b. The total *C*-coupled resistances $R_T = R_{Hf} + R_{Lf}$ are shown in **Figure 8**a as a function of the V_{oc}. R_T follows an exponential law like R_{dc} (15.a) with $m \approx 1.2$, being R_{th} approximately a 20% larger for LIMIS than that from IS, i.e., wider arcs as in **Figure 3**b. Accordingly, from (16): $R \approx 0.6 \cdot R_{IS}$ under illumination.

In addition, the right-shifting Z_s' (see **Figure 3**b) also follows an exponential decrease as (15.a), but with $m \approx 2$, as in **Figure 8**a. This is an extra impedance contribution, different than that of the ohmic R_{series} (nearly constant in **Figure 8**a) which may be detailed studied in the future. Here it is important to note that the high frequency part of the LIMIS spectra is particularly difficult to fit due to the lower linearity of the signal, as expressed in the significance spectra of Figure S3.

The capacitance bode plots are shown in Figure S3 with the respective simulations to **Figure 7**b EC model. The total capacitance $C_T = C_{Hf} + C_{Lf}$ from the fittings is plotted in **Figure 8**b showing an exponential increase possibly due to diffusion capacitance.[35, 40] In this case the C_T from LIMIs is nearly half of that from IS, so from (17): $C \approx 1.5 \cdot C_{IS}$ under illumination.

With the information of R and C, the characteristic times $\tau = RC$ can be accessed, as presented in **Figure 8**c. Note that from (16) and (17) the total time response is actually a 90% of that calculated for IS. **Figure 8**c also present the transient photovoltage (TPV) lifetimes τ which nearly coincides with IS and LIMIS a lower light intensities (below ~3 mW·cm^{-2}). The TPV measurements were performed with a self-made setup (see Section S1.7 for details) in order to contrast the results from the characteristic time constants. As the light intensity is augmented, the TPV signal does not decay exponentially anymore (see Figure S17) and the IS and LIMIS provide a better estimation of characteristic lifetimes. In addition, The LIMIS seems to inform on faster characteristic times (τ_{Hf}), possibly related with charge extraction processes, i.e., not as slow as the recombination lifetime.

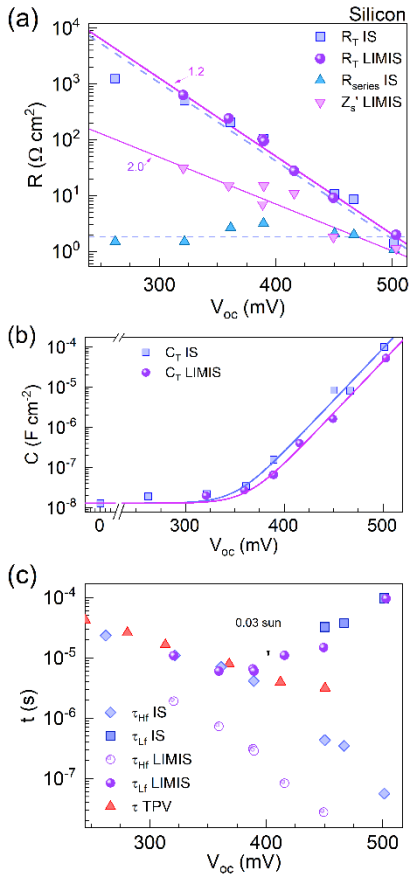

Figure 8. Silicon solar cell numerical simulation results: (a) resistance, (b) capacitance and (c) characteristic times from LIMIS and IS (EC model in **Figure 7**b) and TPV (mono-exponential decay model). The lines in (a) are the fittings to (15.a) with m as indicated with arrows.

For the organic solar cell, **Figure 9**a shows R_T, Z_s' and R_{series} as a function of V_{oc} for the IS and LIMIS spectra, as well as the numerical simulations to the EC model of **Figure 7**b, as presented with solid lines (see Figure S6). The OrgSC displays a more evident trend as $Z_s' \propto \exp[-qV_{oc}/2\,k_BT]$ and R_T also behaves like R_{dc} (15.a) but with $m \approx 1.8$ and R_{th} approximately a 8% larger for LIMIS than that from IS, which gives from (16): $R \approx 0.51 \cdot R_{IS}$ under illumination.

Capacitance spectra are also displayed in Figure S6, and the total capacitance of the OrgSC from the fittings is presented in **Figure 9**b, which is basically C_{Lf}, significantly higher and exponentially increasing in comparison with the constant geometrical capacitance $C_{Hf} = C_g$. In this case LIMIS presents a 64% higher capacitance with respect to LIMIS, so from (16): $C \approx 2.64 \cdot C_{IS}$. Accordingly, the actual total characteristic times may be 1.35 times bigger than they are from IS, which is nearly τ_{Lf} for LIMIS. This result approaches the lifetimes from TPV below $\sim$10 mW·cm^{-2} (see decays in Figure S10) and the characteristic times from IS and LIMIS, as presented in **Figure 4**c. In that figure it is also evident how LIMIS and IS characteristic times are similar for the OrgSC, unlike the SiCS.

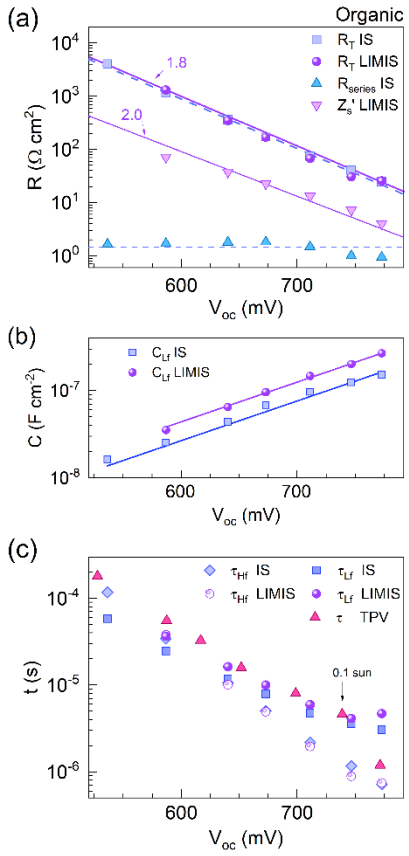

Figure 9. Organic solar cell numerical simulation results: (a) resistance, (b) capacitance and (c) characteristic times from LIMIS and IS (EC model in **Figure 7**b) and TPV (mono-exponential decay model). The lines in (a) are the fittings to (15.a) with m as indicated with arrows.

The perovskite solar cells spectra were simulated with extra resistive and capacitive parameters, now using the EC model of **Figure 7**c. Note that such EC model does not include inductive elements, as earlier needed[33] in devices with similar mixed perovskite absorber but TiO_2 and spiro-OMeTAD as selective contacts. This suggest that the inductive behavior is an electrode-related issue.

The R_T and R_{series} from PSC1 IS spectra is summarized in **Figure 10**a. Note that $R_T \approx R_{Hf}$, meaning that the contributions to resistance from the R_{Lf1} and R_{Lf2} are much lower. But in the case of LIMIS in PSCs, the $R_{Hf}$is mostly replaced by the series-resistance-like parameter Z_s' and the total C-coupled resistances only include

low frequency contributions $R_T \approx R_{Lf1} + R_{Lf1}$. Thus, what makes sense in PSCs is to compare R_T from IS vs. $Z'_{\mathrm{T}} = R_T + Z'_{\mathrm{s}}$ from LIMIS. The resistive fitting parameters are summarized in **Figure 10**a showing R_T and Z'_{T} proportional to $\exp[-qV_{oc}/1.7\ k_BT]$, $Z_s{}' \propto \exp[-qV_{oc}/2.5\ k_BT]$ and R_{series} stepped constant as a function of V_{oc}. Analogously, Z'_{T} from LIMIS is around 15% larger than R_T from IS, so from (16): $R \approx 0.53 \cdot R_{IS}$ under illumination.

More interestingly are the capacitive features and the resulting time constants. In **Figure 10**b, we show low frequency capacitances C_{Hf1} and C_{Hf2} as resulted from the numerical fitting to the EC model of **Figure 7**c. The trend $C_{Hf1} \propto \exp[qV_{oc}/1.5k_BT]$ has been earlier reported as a distinctive feature in mixed cations perovskite based solar cells with TiO_2 and spiro-OMeTAD as selective contacts.[33, 35] However, the even higher and saturating-like $C_{Hf2} \propto \exp[qV_{oc}/5k_BT]$ is a new finding. C_{Hf2} may be connected to the modification of interface contact with the SnO_2 and/or the PDCBT and the types of cations composing the absorber layer. This adds extra elements to the already anomalous capacitive response of PSCs, closely connected with the $J-V$ curve hysteretic behaviors.[2, 41] Importantly, LIMIS and IS both nearly reproduce the same capacitances, which reinforce the idea of interconnected ionic-electronic nature of these slower mechanisms.

The characteristic response times are summarized in **Figure 10**c. The high frequency times follow the resistance trend and even approximately agree with the TPV lifetimes (see decays in Figure S14). The low frequency times behave slightly constant and decreasing, τ_{Hf1} and τ_{Hf1} respectively, suggesting an eventual convergence around miliseconds.

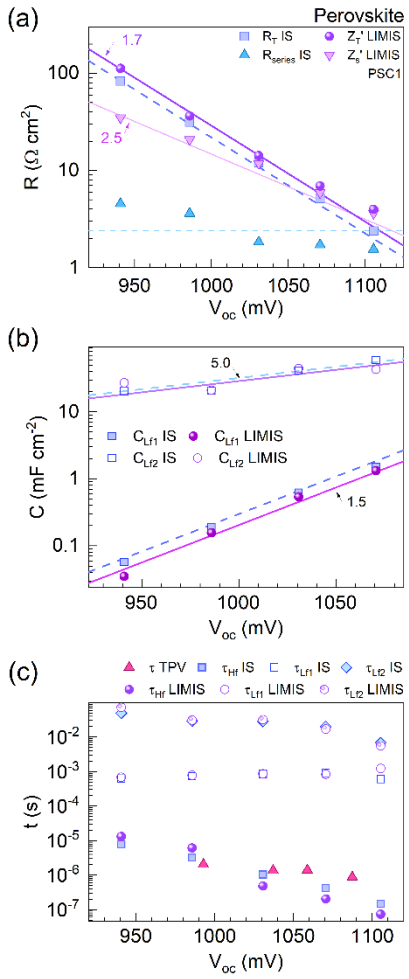

Figure 10. Perovskite solar cell (PSC1) numerical simulation results: (a) resistance, (b) capacitance and (c) characteristic times from LIMIS and IS (EC model in **Figure 7**c) and TPV (mono-exponential decay model). The lines in (a) are the fittings to the R_{dc} behavior with m as indicated with arrows. The lines in (a) are the fittings to (15.a) with m as indicated with arrows.

Two more perovskite solar cells PSC2 and PSC3 were analyzed as summarized in Sections S1.5 and S1.6, respectively, with nearly similar trends to PSC1. Nevertheless, regarding the low frequency capacitance, by eliminating the PMMA/PCBM cover towards the SnO_2 in PSC2, we obtain almost totally saturated $C_{Hf} = C_{Hf2}$ and discrepancies between LIMIS and IS (see Figure S13b), converging as light intensity increases. On the other hand, typical $C_{Hf} = C_{Hf1} \propto \exp[qV_{oc}/1.5k_BT]$ is again obtained if, with the same electrodes as PSC2, the methylamonium and Bromide

compositions are neglected, as in PSC3 (see Figure S16b). The detailed analysis of these features, while only reported here, should be attended in future studies.

2.4. Bias-dependent photocurrent correction to the empirical Shockley equation around open circuit

From the previous section it was stated how the LIMIS spectra, despite resembling the IS shapes, are not the same as the IS spectra. This result from the spectroscopic *ac* characterization is also in agreement with the *dc* response in Section S1.8. In Figure S18 the experimental *J-V* curves from three of the studied samples (SiSC, OrgSC and PSC1) are presented as a function of the illumination intensity, forming current three-dimensional (3D) surfaces. The corresponding short-circuit currents are displayed in Figure S19 confirming the well-known relation $J_{sc} \propto P_{in}$ at $V = 0$ as (4.b).

From the experimental data in Figure S19 we can numerically find the pair (V, P_{in}) for the current roots (OC) and calculate the numerical derivatives for IS, IMPS and IMVS as (11). The code for that calculus is in Table S2 and the results are shown in **Figure 11** comparing IS and LIMIS as *dc* resistances. For the SiSC, IS and LIMIS coincide only at the highest illumination intensities, where $R_{dc} \propto {P_{in}}^{-1}$ agrees with **Figure 3**a suggesting light independent Ψ_J and $P_{in} = J_s \exp[qV/mk_BT]$ from the empirical Shockley equation (4). For samples OrgSC and PSC1(and SiSC at lower P_{in}) the R_{dc} is more evidently different from IS and LIMIS. Particularly, the "S" shape of OrgSC above OC creates a remarkable difference between IS and LIMIS. Interestingly, different trends $R_{dc} \propto {P_{in}}^{-b}$ are found depending on the sample and the illumination intensity range.

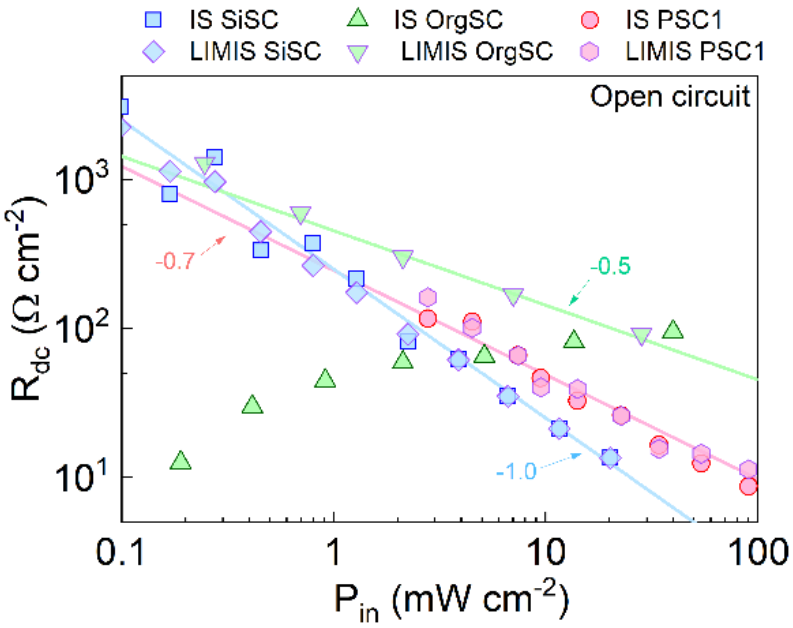

Figure 11. Numerically calculated *dc* resistances at OC using the differential definitions of IS and LIMIS on experimental $J-V$ curves at different light intensities. The experimental data is plotted in Figure S21 and the calculation code in Table S2.

The above experimental observations contradict the formulation of the well-known empirical Shockley equation (4) when applying the LIMIS definition (9) as in (15). Note first that we already showed Ψ_J decreasing with light intensity at OC (see **Figure 4**a, **Figure 5**a, Figure S11d and Figure S14d), but at SC it still agrees with (4), as in Figure S19. Accordingly, a correction in (4.a) may be introduced justifying to apply the IMPS differential definition (11.b) at OC to obtain a decrease of Ψ_J as P_{in} increase. This correction makes sense only if a bias-dependency $\Psi_J(V)$ is included.

The deviations from the superposition principle in a form of bias-dependent photocurrent are well reported issues in silicon,[42, 43] thin film[44-47] and organic[48-50] solar cells. Another related subject is the *ac*/*dc* photo-shunting[51, 52] at SC, also reported for PSCs.[2, 35, 53] These are still open problems, which have been approached in several

ways. In practice, under illumination both the photogenerated as well as recombination and drift-diffusion current components are modified by the field profile. Thus, only by numeric simulations the actual collection efficiency can be evaluated. Nevertheless, it is customary to still neglect changes in the dark diode term in (4) and group all the corrections to the model in the J_{ph} term, which can be experimentally accessed from the difference between dark and illuminated $J-V$ curves. In this direction, an empirical formulation would be

$$J_{ph} \cong J_{sc}\left(\varsigma + \frac{\varsigma - 1}{1+\exp\left[\frac{q\left(V-V_{\varsigma}\right)}{m_{\Psi}k_{B}T}\right]}\right) \tag{18}$$

with $J_{sc} = P_{in}\Psi_{sc}$, the collection fraction ς, the collection threshold voltage V_{ς} and $m_{\Psi} > m$ is the photocurrent ideality factor. Here V_{ς} indicates the critical bias above which the J_{sc} loses are more than half. Since the flat-band condition is particularly detrimental for the charge extraction, it makes sense to approach it to the built-in voltage $V_{\varsigma}{\sim}V_{bi}$. The parameter ς signifies how much photocurrent holds upon bias increasing: $\varsigma = 1$ means no loses, $\varsigma = 0$ indicate loss of entire J_{sc} and $\varsigma < 0$ implies a crossing between light and dark $J-V$ curves (see Figure S20a). The step-like expression (18) successfully describes most of the experimental behaviours, but it precludes finding an analytical expression for the V_{oc} analogue to (4.b) to calculate derivatives as (11). However, our evidence and general focus is only around the OC regime, thus, what makes sense is to approximate (18)

Particularly from our observations around OC we can empirically approximate

$$\Psi_J = \Psi_{oc}\exp\left[-\frac{qV}{m_\Psi k_B T}\right] \tag{19}$$

where $\Psi_{oc} \approx \Psi_{sc}\exp\left[qV_\varsigma/m_\Psi k_B T\right]$ is the current permittivity at OC. With this assumption, the corrected empirical Shockley equation around OC should be reformulated as

$$J \cong J_s\left(\exp\left[\frac{qV}{m\,k_B T}\right]-1\right) - P_{in}\Psi_{oc}\exp\left[-\frac{qV}{m_\Psi k_B T}\right] \tag{20}$$

Equation (20) successfully reproduces the photocurrent around V_{oc}, as illustrated in Figure S20b,c. Hence, we can rewrite (15) for OC condition (see deductions in Section S2.2) as

$$R_{dc} = R_{th}\exp\left[-\frac{qV_{oc}}{m\,k_B T}\right]\left(\frac{1}{1+\frac{m}{m_\Psi}r_\Psi(V)}\right) \tag{21.a}$$

$$\Psi_{J,dc} = -\Psi_{oc}\exp\left[-\frac{qV_{oc}}{m_\Psi k_B T}\right] \tag{21.b}$$

$$\Psi_{V,dc} = \frac{m_\Psi}{(m_\Psi + m)}\frac{m\,k_B T}{q\,P_{in}} \tag{21.c}$$

$$R_{\Psi,dc} = R_{th}\exp\left[-\frac{qV_{oc}}{mk_B T}\right]\left(\frac{1}{1+\frac{m}{m_\Psi}}\right) \tag{21.d}$$

where the photocurrent resistance factor r_Ψ comes after (S6), resulting $r_\Psi > 1$ for low illumination intensities before $r_\Psi \to 0$ when $V_{oc} \to V_{bi}$.

Note that (21) explains the three main experimental observations. First, the decrease trends of Ψ_J and Ψ_V as P_{in} is augmented at OC in (21b,c) agree with the low frequency

limits of IMPS and IMVS spectra, respectively. Second, from the parentheses in (21a,d) we see that $R_{\Psi,dc} \geq R_{dc}$, as the experimental evidence discussed in the previous section. And third, by comparing IS and LIMIS *dc* resistances we realize that they converge only when $m_\Psi \gg m$, so both parentheses in (21a,d) equal unity, and as V_{oc} increases, as suggested more evidently by the SiSC behavior in **Figure 6** and **Figure 11**.

3. Conclusions

In summary, the concept and initial theoretical considerations for a new method of characterization of all-solid-state solar cells were presented: the light intensity modulated impedance spectroscopy (LIMIS). Differently to the standard potentiostatic impedance spectroscopic (IS), LIMIS perturbates photo-sensitives samples with light and the photocurrent and photovoltage signals are recorded and analyzed.

Preliminary LIMIS spectra measurements were presented and compared with IS spectra, resulting similar in shape but in most of the cases the total impedance from LIMIS exceeds that from IS. That difference is first analyzed as potential figure of merit for evaluation performance and degradation of solar cells. Those results and the light dependency of the current responsivity at open circuit justified a correction to the empirical Shockley equation, including a bias dependent photo-current term.

Moreover, it has been shown how the total differential resistances and capacitances are reduced and augmented, respectively with respect to IS, illustrating the photoconductivity increase under illumination for the solar cells. This effect corrects

the evaluation of the lifetimes, which is a factor to consider in the typical differences when evaluating that parameter by different techniques, like TPV.

Conflicts of interest

There are no conflicts to declare.

Acknowledgements

We thank Ministerio de Ciencia, Innovación y Universidades of Spain under project (MAT2016-76892-C3-1-R). O.A. acknowledges the financial support from the VDI/VD Innovation + Technik GmbH (Project-title: PV-ZUM) and the SAOT funded by the German Research Foundation (DFG) in the framework of the German excellence initiative.

AUTHOR INFORMATION

Corresponding Author

*E-mail: osbel.almora@fau.de

ORCID

Osbel Almora: 0000-0002-2523-0203

Germà Garcia-Belmonte: 0000-0002-0172-6175

Christoph J. Brabec: 0000-0002-9440-0253

References

1. J. Bisquert and F. Fabregat-Santiago, in *Dye-sensitized solar cells*, ed. K. Kalyanasundaram, CRC Press, Lausanne (Switzerland), 2010, ch. 12, pp. 457-487.

2. P. Lopez-Varo, J. A. Jiménez-Tejada, M. García-Rosell, S. Ravishankar, G. Garcia-Belmonte, J. Bisquert and O. Almora, *Adv. Energy Mater.*, 2018, **8**, 1702772.
3. E. Kamieniecki, *J. Vac. Sci. Technol.*, 1982, **20**, 811-814.
4. E. Kamieniecki, *J. Appl. Phys.*, 1983, **54**, 6481-6487.
5. R. Peat and L. M. Peter, *J. Electroanal. Chem. Interfacial Electrochem.*, 1987, **228**, 351-364.
6. E. A. Ponomarev and L. M. Peter, *J. Electroanal. Chem.*, 1995, **396**, 219-226.
7. L. Dloczik, O. Ileperuma, I. Lauermann, L. M. Peter, E. A. Ponomarev, G. Redmond, N. J. Shaw and I. Uhlendorf, *J. Phys. Chem. B*, 1997, **101**, 10281-10289.
8. P. E. de Jongh and D. Vanmaekelbergh, *J. Phys. Chem. B*, 1997, **101**, 2716-2722.
9. G.-O. Kim, *Bull. Korean Chem. Soc.*, 2012, **33**, 469-472.
10. A. Pockett, G. E. Eperon, T. Peltola, H. J. Snaith, A. Walker, L. M. Peter and P. J. Cameron, *J. Phys. Chem. C*, 2015, **119**, 3456-3465.
11. Y. Gao, A. J. Wise, A. K. Thomas and J. K. Grey, *ACS Appl. Mater. Interfaces*, 2016, **8**, 285-293.
12. L. Bertoluzzi and J. Bisquert, *J. Phys. Chem. Lett.*, 2017, **8**, 172-180.
13. S. Ravishankar, C. Aranda, S. Sanchez, J. Bisquert, M. Saliba and G. Garcia-Belmonte, *J. Phys. Chem. C*, 2019, **123**, 6444–6449.
14. S. Ravishankar, A. Riquelme, S. K. Sarkar, M. Garcia-Batlle, G. Garcia-Belmonte and J. Bisquert, *J. Phys. Chem. C*, 2019, **123**, 24995-25014.
15. J. Krüger, R. Plass, M. Grätzel, P. J. Cameron and L. M. Peter, *J. Phys. Chem. B*, 2003, **107**, 7536-7539.
16. Y. T. Set, B. Li, F. J. Lim, E. Birgersson and J. Luther, *Appl. Phys. Lett.*, 2015, **107**, 173301.
17. X. Chen, Y. Shirai, M. Yanagida and K. Miyano, *Phys. Chem. Chem. Phys.*, 2018, **20**, 17918-17926.
18. S. Ravishankar, C. Aranda, P. P. Boix, J. A. Anta, J. Bisquert and G. Garcia-Belmonte, *J. Phys. Chem. Lett.*, 2018, **9**, 3099-3104.
19. Q. Cui, X. Zhao, H. Lin, L. Yang, H. Chen, Y. Zhang and X. Li, *Nanoscale*, 2017, **9**, 18897-18907.
20. D. Prochowicz, M. M. Tavakoli, A. Q. Alanazi, S. Trivedi, H. Tavakoli Dastjerdi, S. M. Zakeeruddin, M. Grätzel and P. Yadav, *ACS Omega*, 2019, **4**, 16840-16846.
21. H. Song and D. D. Macdonald, *J. Electrochem. Soc.*, 1991, **138**, 1408-1410.
22. J. Halme, *Phys. Chem. Chem. Phys.*, 2011, **13**, 12435-12446.
23. O. Almora, D. Miravet, G. J. Matt, G. Garcia-Belmonte and C. J. Brabec, *J. Appl. Phys.*, 2019, **submitted**, https://arxiv.org/abs/1910.05031.
24. M. A. Green, *Solar Cells. Operating principles, Technology and System Applications*, Prentice-Hall, 1982.
25. X. Du, T. Heumueller, W. Gruber, A. Classen, T. Unruh, N. Li and C. J. Brabec, *Joule*, 2019, **3**, 215-226.
26. J. Yuan, Y. Zhang, L. Zhou, G. Zhang, H.-L. Yip, T.-K. Lau, X. Lu, C. Zhu, H. Peng, P. A. Johnson, M. Leclerc, Y. Cao, J. Ulanski, Y. Li and Y. Zou, *Joule*, 2019, **3**, 1140-1151.

27. J. Wei, F. Guo, X. Wang, K. Xu, M. Lei, Y. Liang, Y. Zhao and D. Xu, *Adv. Mater.*, 2018, **30**, 1805153.
28. O. Almora, L. Vaillant-Roca and G. Garcia-Belmonte, *Rev. Cubana Fis.*, 2017, **34**, 58-68.
29. J. Li and L. M. Peter, *J. Electroanal. Chem. Interfacial Electrochem.*, 1985, **193**, 27-47.
30. J. C. Byers, T. Heiser, M. Skorobogatiy and O. A. Semenikhin, *ACS Appl. Mater. Interfaces*, 2016, **8**, 28789-28799.
31. O. Almora, M. García-Batlle and G. Garcia-Belmonte, *J. Phys. Chem. Lett.*, 2019, **10**, 3661-3669.
32. C. A. Schiller and R. Kaus, *ECS Transactions*, 2010, **25**, 49-62.
33. O. Almora, K. T. Cho, S. Aghazada, I. Zimmermann, G. J. Matt, C. J. Brabec, M. K. Nazeeruddin and G. Garcia-Belmonte, *Nano Energy*, 2018, **48**, 63-72.
34. W. Tress, M. Yavari, K. Domanski, P. Yadav, B. Niesen, J. P. Correa Baena, A. Hagfeldt and M. Graetzel, *Energy Environ. Sci.*, 2017, **11**, 151-165.
35. O. Almora and G. Garcia-Belmonte, *Solar Energy*, 2019, **189**, 103-110.
36. O. Almora, C. Aranda and G. Garcia-Belmonte, *J. Phys. Chem. C*, 2018, **122**, 13450-13454.
37. C. Donolato, *Appl. Phys. Lett.*, 1985, **46**, 270-272.
38. P. P. Boix, J. Ajuria, R. Pacios and G. Garcia-Belmonte, *J. Appl. Phys.*, 2011, **109**, 074514.
39. A. Todinova, L. Contreras-Bernal, M. Salado, S. Ahmad, N. Morillo, J. Idígoras and J. A. Anta, *ChemElectroChem*, 2017, **4**, 1-12.
40. O. Almora, L. G. Gerling, C. Voz, R. Alcubilla, J. Puigdollers and G. Garcia-Belmonte, *Sol. Energy Mater. Sol. Cells*, 2017, **168**, 221-226.
41. O. Almora, P. Lopez-Varo, K. T. Cho, S. Aghazada, W. Meng, Y. Hou, C. Echeverría-Arrondo, I. Zimmermann, G. J. Matt, J. A. Jiménez-Tejada, C. J. Brabec, M. K. Nazeeruddin and G. Garcia-Belmonte, *Sol. Energy Mater. Sol. Cells*, 2019, **195**, 291-298.
42. S. S. Hegedus, *Prog. Photovoltaics*, 1997, **5**, 151-168.
43. D. S. H. Chan, J. C. H. Phang and H. W. Wong, *Solid-State Electron.*, 1987, **30**, 919-925.
44. M. Eron and A. Rothwarf, *Appl. Phys. Lett.*, 1984, **44**, 131-133.
45. J. E. Moore, S. Dongaonkar, R. V. K. Chavali, M. A. Alam and M. S. Lundstrom, *IEEE J. Photovoltaics*, 2014, **4**, 1138-1148.
46. S. Hegedus, D. Desai and C. Thompson, *Prog. Photovoltaics*, 2007, **15**, 587-602.
47. M. Gloeckler, C. R. Jenkins and J. R. Sites, *MRS Proceedings*, 2003, **763**, B5.20.
48. W.-I. Jeong, J. Lee, S.-Y. Park, J.-W. Kang and J.-J. Kim, *Adv. Funct. Mater.*, 2011, **21**, 343-347.
49. G. F. A. Dibb, T. Kirchartz, D. Credgington, J. R. Durrant and J. Nelson, *J. Phys. Chem. Lett.*, 2011, **2**, 2407-2411.
50. M. Lenes, M. Morana, C. J. Brabec and P. W. M. Blom, *Adv. Funct. Mater.*, 2009, **19**, 1106-1111.
51. C. Voz, J. Puigdollers, J. M. Asensi, S. Galindo, S. Cheylan, R. Pacios, P. Ortega and R. Alcubilla, *Org. Electron.*, 2013, **14**, 1643-1648.

52. W. Tress, K. Leo and M. Riede, *Phys. Status Solidi RRL*, 2013, **7**, 401-405.
53. I. Zarazua, G. Han, P. P. Boix, S. Mhaisalkar, F. Fabregat-Santiago, I. Mora-Seró, J. Bisquert and G. Garcia-Belmonte, *J. Phys. Chem. Lett.*, 2016, **7**, 5105-5113.